

# SCIENTIFIC RETURN OF CORONAGRAPHIC EXOPLANET IMAGING AND SPECTROSCOPY USING WFIRST

ADAM BURROWS<sup>1</sup>

*Draft version July 4, 2018*

## ABSTRACT

In this study, we explore and review the scientific potential for exoplanet characterization by a high-contrast optical coronagraph on WFIRST/AFTA. We suggest that the heterogeneity in albedo spectra and planet/star flux ratios as a function of orbital distance, planet mass, and composition expected for the giant exoplanets at separations from their primaries accessible to WFIRST will provide unique constraints on giant planet atmospheres, evolution, aerosol and cloud properties, and general theory. Such exoplanets are not merely extrapolations of Jupiter and Saturn, but are likely to occupy a rich continuum of varied behaviors. Each in themselves and jointly, optical spectra, photometry, and polarization measurements of a diverse population of giant exoplanets in the solar neighborhood has the potential to reveal a multitude of fundamental features of their gas-giant chemistry, atmospheres, and formation. Such a campaign will enrich our understanding of this class of planets beyond what is possible with even a detailed exploration of the giants in our own solar system, and will compliment ongoing studies of exoplanets in the infrared and on close-in orbits inaccessible to coronagraphy.

## 1. INTRODUCTION

Exoplanet science is observational and must rely on the astronomical tools of remote spectroscopic sensing to infer the physical properties of individual planets and their atmospheres. Therefore, there is a premium on obtaining *spectra* and on improving sensitivity, without the luxury of the direct, in-situ probes employed so profitably in our solar system.

Before the successful emergence of the RV (radial-velocity) and transit methods, astronomers expected high-contrast direct imaging, that separated out the light of planet and star and provided photometric and spectroscopic data for each, would be the leading means of exoplanet discovery and characterization. A few wide-separation brown dwarfs and/or super-Jupiter planets were detected by this means, but the yield was meager. The fundamental problem is two-fold: 1) the planets are intrinsically dim, and 2) it is difficult to separate out the light of the planet from under the glare of the star for planet-star separations like those of the solar system. Imaging systems need to suppress the stellar light scattered in the optics that would otherwise swamp the planet's signature. The planet/star contrast ratio for Jupiter is  $\sim 10^{-9}$  in the optical and  $\sim 10^{-7}$  in the mid-infrared. For Earth, the corresponding numbers are  $\sim 10^{-10}$  and  $\sim 10^{-9}$ . These numbers are age, mass, orbital distance, and star dependent, but demonstrate the challenge. What is more, contrast capabilities are functions of planet-star angular separation, restricting the orbital space accessible.

However, things are changing. Recently, giant exoplanets and brown dwarfs such as HR 8799bcde,  $\beta$ -Pictoris b, GQ Lup b, 2MASS 1207b, and GJ 504b have been discovered and partially characterized using near-IR high-contrast techniques. The HR 8799 (Marois et al. 2008, 2010; Barman et al. 2011) and  $\beta$ -Pictoris b

(Lagrange et al. 2009) giant planets/brown dwarfs have masses of  $\sim 5 - 15$  Jupiter masses ( $M_J$ ) and angular separations between  $\sim 0.3$  and  $\sim 1.5$  arcseconds. Their contrast ratios in the near infrared are  $\sim 10^{-4}$ , but capabilities near  $10^{-5}$  have been achieved. Such direct imaging is currently most sensitive to wider-separation ( $\sim 10-200$  AU), younger, giant exoplanets (and brown dwarfs). Fortunately, with the advent of the ground-based GPI (on Gemini) (Macintosh et al. 2008), LBTI (Skrutskie et al. 2010), SPHERE (on the VLT) (Beuzit et al. 2008), and ScExAO/Charis/HiCIAO (on Subaru) (Suzuki et al. 2010) and the space-based NIRC2 and MIRI on JWST (Deming et al. 2009; Shabram et al. 2009), more capable high-contrast imaging with near-IR performance perhaps as good as  $10^{-7}$  for  $\sim 1.0$  AU separations for nearby stars ( $\leq 10$  parsecs) will soon be routine.

All this recent high-contrast activity is for measurements only in the infrared. However, albedos, phase functions, and polarization measurements in the optical have a long tradition in solar-system studies, and great potential to constrain exoplanet compositions, Keplerian elements, and aerosol and cloud properties (Marley et al. 1999). Hence, there is excitement surrounding the possibility that an optical coronagraph (CGI) will be put on the Wide-Field Infrared Survey Telescope (WFIRST)/Astrophysics Focused Telescope Assets (AFTA) mission<sup>2</sup>. It is being designed to achieve

<sup>2</sup> One of the stated priorities of NASA's Science Mission Directorate is to study and characterize exoplanets. Two of the science goals highlighted in its 2014 *Science Plan* are to "Explore the origin and evolution of the galaxies, stars, and *planets* that make up our universe" and to "Discover and study planets around other stars, ..." In the past, NASA has profitably and strategically invested in platforms, such as HST, *Spitzer*, the Keck telescopes, and *Kepler*, to expand our knowledge of exoplanets. In the future, it plans to launch JWST, and to participate in the near- and mid-IR SPICA mission. Moreover, the NRC's 2010 decadal survey of astronomy and astrophysics, "New Worlds, New Horizons" (NWNH), gave WFIRST the highest priority for a new large space mission. In addition to the science and payload originally envisioned for WFIRST by NWNH, NASA is now considering an

<sup>1</sup> Department of Astrophysical Sciences, Peyton Hall, Princeton University, Princeton, NJ 08544; burrows@astro.princeton.edu

optical ( $\sim 0.4\text{--}1.0\ \mu\text{m}$ ) planet/star contrast ratios better than  $\sim 10^{-9}$  (Spergel et al. 2013) (with an inner-working-angle (IWA) near to or better than  $\sim 0.2''$ ) and some capability to measure linear polarization, though perhaps only for the imager. Figure 1 compares the expected achievable planet/star contrast ratio of WFIRST/CGI in the optical with the corresponding expected or demonstrated ratios for GPI, HST, and JWST in the near-infrared, and makes clear the quantum leap in capability WFIRST/CGI represents.

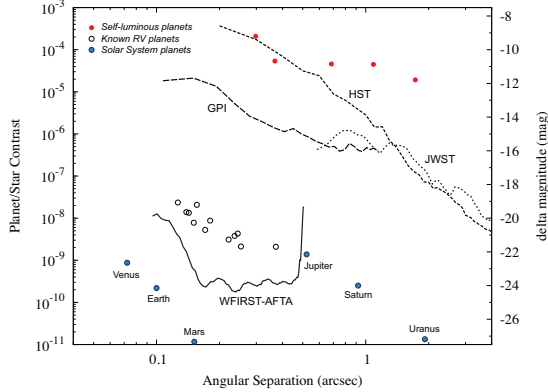


FIG. 1.— Comparison of the expected planet/star contrast sensitivities of JWST, GPI, SPHERE (all in  $H$  band), and WFIRST/CGI (in the optical). The equivalent magnitude difference is provided on the right vertical axis. Various comparison objects are included for reference. Figure is taken from Spergel et al. (2013).

A low-resolution ( $R = \lambda/\Delta\lambda \sim 70$ ) IFS spectrometer is part of the baseline coronagraph design. A jupiter-mass planet in a 4-AU orbit about a G2V star at 10 parsecs has an angular separation as large as  $0.4''$ , and just beyond greatest elongation (in a gibbous phase) it is expected at an age of  $\sim 5$  Gyrs to exhibit optical planet/star contrasts above  $\sim 2 \times 10^{-9}$ . Even at 6 AU, and at this same phase, the planet-star contrast in the optical is expected to be roughly  $10^{-9}$ . For young and/or massive giant exoplanets, the contrasts are much higher. The optical has prominent methane features near  $\sim 0.62\ \mu\text{m}$ ,  $\sim 0.74\ \mu\text{m}$ ,  $\sim 0.81\ \mu\text{m}$ , and  $\sim 0.89\ \mu\text{m}$ , ammonia has spectral bands at  $\sim 0.65\ \mu\text{m}$  and  $\sim 0.79\ \mu\text{m}$ , and there is a broad water band at  $\sim 0.94\ \mu\text{m}$ . Rayleigh scattering off molecules and Mie-like scattering off cloud particulates and hazes can modify planet reflectivity in diagnostic ways. A coronagraph on WFIRST/AFTA would be uniquely suited to provide low-resolution optical albedo spectra for giant exoplanets, brown dwarfs, and some exoNeptunes at unprecedented contrast ratios.

In this monograph, we summarize the theory of the wavelength-dependent reflection albedos, phase functions, and polarizations as a function of 1) an exoplanet's mass, age, and composition, and 2) its Keplerian elements (including orbital distance). This work is meant to highlight the great diagnostic potential for

optional addition of a coronagraph for direct imaging and low-resolution spectroscopy of giant and Neptune-like exoplanets and brown dwarfs. This new departure has been enabled by the transfer from the National Reconnaissance Office of two 2.4-meter space telescopes, one of which is being contemplated for a WFIRST with greatly augmented capabilities.

giant exoplanet characterization using the anticipated optical imaging and spectrophotometric coronagraph on WFIRST. Low-resolution spectra and polarimetry in the optical can be used to constrain the atmospheric abundances of methane and water, and the character, pressure levels, and physical properties of clouds and hazes expected in giant planet atmospheres. We suggest that there should be significant variation in the signatures of different giant exoplanets, and that Jupiter and Saturn may not be apt templates for all giant exoplanets at wide separations amenable to high-contrast measurement.

## 2. OPTICAL REFLECTION FROM GAS-GIANT PLANETS: FORMALISM

For a planet at wide orbital separation from its parent star, the planet/star contrast ratio in the optical and the associated geometric albedo ( $A_g(\lambda)$ ) are the measurement goals. They are related by the formula:

$$\frac{F_p}{F_*} = A_g(\lambda) \left( \frac{R_p}{a} \right)^2 \Phi(\alpha), \quad (1)$$

where  $\lambda$  is the photon wavelength,  $\Phi(\alpha)$  is a function of orbital phase angle ( $\alpha$ ),  $R_p$  is the planet's radius, and  $a$  is its orbital distance.  $A_g(\lambda)$  contains much of the information on the atmosphere's composition, pressure, and cloud/haze profiles, though  $\Phi(\alpha)$  also contains information on the atmosphere's scattering characteristics. The scattering albedo ( $\omega(\lambda)$ ) for single scattering off the constituents of the atmosphere is a function of wavelength and composition and is the ratio of the scattering cross section to the total cross section. For a homogeneous atmosphere,  $A_g(\lambda)$  is a direct function of  $\omega(\lambda)$ . Individual scattering phase functions for single scattering can be complicated, particularly for cloud and haze particles (for which the Mie theory is often employed), but can generally be modeled using the Henyey-Greenstein scattering phase function:

$$p(\Theta) = \frac{1 - g^2}{(1 + g^2 - 2g \cos \Theta)^{3/2}}, \quad (2)$$

or the anisotropic phase function:

$$p(\Theta) = 1 + 3g \cos \Theta, \quad (3)$$

where  $\Theta$  is the single scattering angle and  $g = \langle \cos \Theta \rangle$ . Though the phase functions for Mie scattering are more complicated, the anisotropic phase functions above, employing only the average  $g$  and assuming a simple cosine angular dependence, can oftentimes suffice for calculating reliable geometric albedos.

The scalar Rayleigh phase function for scattering off individual molecules is:

$$p(\cos \Theta) = \frac{3}{4}(1 + \cos^2 \Theta). \quad (4)$$

However, vector Rayleigh scattering, with the full polarization matrix, is a more accurate representation of Rayleigh scattering. One difference is that, while  $A_g = 0.75$  for scalar Rayleigh scattering, it is 0.7977 for vector Rayleigh scattering, a  $\sim 6\%$  difference.

A fit to  $A_g$  for non-conservative vector Rayleigh scattering in semi-infinite atmospheres is:

$$A_g = 0.7977 \frac{(1 - 0.23s)(1 - s)}{(1 + 0.72s)(0.95 + 0.08\omega)}, \quad (5)$$

where  $s = \sqrt{1 - \omega}$  (Madhusudhan & Burrows 2011). The fit for  $A_g$  is accurate to within 1% for  $\omega \lesssim 0.99$ .

Both Rayleigh and Mie scattering can result in significant polarization of the reflected component ( $\sim 5\text{--}100\%$ ), even after multiple scattering, suggesting that full linear Stokes polarization measurements might be useful for planet and planet orbit characterization (see §2.2 and §5).

In any case, the net effect of an atmospheric layer on the emergent intensity is the weighted sum of the contributions from molecules (Rayleigh) and from aerosols of whatever kind. The products are the measured quantities  $A_g(\lambda)$  and  $\Phi(\alpha)$ . Samples of derived phase functions,  $\Phi(\alpha)$ , for scalar and vector Rayleigh, Lambert reflection, and isotropic scattering are given in Figure 2. Inverting measurements of these quantities yields the physical and compositional characteristics of a planet’s atmosphere, the paramount scientific goals of high-contrast imaging in the optical.

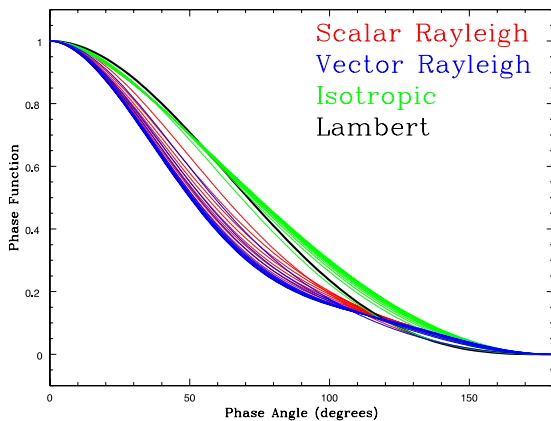


FIG. 2.— Comparison of phase curves for different scattering phase functions. The phase curves for Rayleigh scattering (both scalar and vector) and isotropic scattering are shown for several  $\omega$  values between 0 and 1; higher phase curves correspond to larger  $\omega$ . For Lambert scattering, the phase curve is independent of  $\omega$ . Note that the various phase curves in Figure 2 can differ between phase angles of  $\sim 50^\circ$  and  $\sim 70^\circ$  by more than a factor of two. Figure taken from Madhusudhan & Burrows (2011).

### 2.1. Keplerian Elements

The aspect of a planet in its orbit seen from the Earth depends upon its Keplerian orbital elements. In addition to the time ( $t$ ), these are the planet’s orbital angle/true anomaly ( $\theta$ ), orbit inclination ( $i$ ), eccentricity ( $e$ ), argument of periape ( $\omega_p$ ), longitude of the ascending node ( $\Omega$ ), and period ( $T$ ).<sup>3</sup> The orbital inclination with respect to the reference plane of the sky ranges from  $0^\circ$  for

<sup>3</sup> Note that  $\Omega$  is necessary when a celestial (absolute) frame is designated, (as when measuring full Stokes polarization or cataloguing many different systems in the same solar-system frame), but not when the system itself is allowed to provide a natural orientation, as in the field of radial-velocity planet measurement. In the latter case,  $\Omega = 90^\circ$  can be assumed, or it can be ignored.

fully face-on orbits to  $90^\circ$  for edge-on orbits. The argument of periape is the angular distance measured along the orbit from the line of nodes to periape, where the line of nodes is the intersection of the sky reference plane and the orbital plane of the planet.

A planet’s eccentric anomaly ( $E$ ) can be expressed in terms of its true anomaly using:

$$\sin E = \frac{\sin \theta \sqrt{1 - e^2}}{1 + e \cos \theta}, \quad (6)$$

and its true anomaly is related to its mean anomaly ( $M = 2\pi(t - t_p)/T$ ) using:

$$M = E - e \sin E. \quad (7)$$

Here,  $t_p$  is time of pericenter passage. We can then relate the planet’s orbital angle/true anomaly ( $\theta$ ), as measured from periape, to the orbit time ( $t$ ):

$$t = \frac{T}{2\pi} \left[ 2 \tan^{-1} \left( \sqrt{\frac{1 - e}{1 + e}} \tan \frac{\theta}{2} \right) - \frac{e \sin \theta \sqrt{1 - e^2}}{1 + e \cos \theta} \right]. \quad (8)$$

(We have assumed that  $t = 0$  at pericenter passage.) In this way, the planetary phase curve  $\Phi(\alpha)$  can be expressed as  $\Phi(t)$ , obtaining a true light curve.

In general, the phase angle ( $\alpha$ ) is related to the orbital angle ( $\theta$ ), the argument of periape ( $\omega_p$ ), and the inclination ( $i$ ) by,

$$\cos(\alpha) = \cos(\theta + \omega_p) \sin(i). \quad (9)$$

(Here, we use a particular convention for the orbit orientation:  $\theta = \alpha = 0$  when  $\omega_p = 0$  and  $i = 90^\circ$ .) By combining eq. (8) and (9), we obtain the exact phase of any orbit at any time. The range of observed phase angles,  $\alpha$ , is given by  $90^\circ - i < \alpha < 90^\circ + i$ . Note that even when  $i = 0$  the light curve can vary with time and phase if the orbit is eccentric. In this case,  $a$  (the orbital distance) changes along the orbit (eq. 1).

Though it can be presumed that the astrometry mission *Gaia* will have provided the Keplerian elements for many of the targets of WFIRST/CGI by the time it is launched, it should be noted that both the light curves and the polarization light curves derived using WFIRST could be used for orbit determination as well. In particular, the Stokes polarization vector versus time depends sensitively on the orbital inclination (Fluri & Berdyugina 2010).

### 2.2. Polarization Basics

The Stokes vector is a four-element vector which describes the intensity and polarization of a beam of light, and is represented as  $\mathbf{I} = [I \ Q \ U \ V]$ . Here,  $I$  is the total intensity,  $Q$  and  $U$  are components of intensities with linear polarization, and  $V$  is the intensity with circular polarization. For exoplanets, we can generally ignore  $V$ .

The degree of polarization ( $P$ ) is defined as  $P = \sqrt{Q^2 + U^2}/I$ . For edge-on orbits, however, the disk-integrated Stokes  $U$  vanishes due to symmetry in the north-south direction, in which case  $P = Q/I$ . In general, the angle of polarization is defined as  $\theta_P = \frac{1}{2} \tan^{-1}(U/Q)$ . As a generalization of eq. (1), normalized to the stellar flux, we have for edge-on orbits:

$$Q'(\theta) = A_g \left( \frac{R_p}{a} \right)^2 \Phi(\alpha) P(\theta), \quad (10)$$

where  $\theta$  is the orbital phase/true anomaly,  $\Phi(\alpha)$  is the phase function, and  $P(\theta)$  is the fractional degree of polarization.  $Q'$  is defined in the orbital plane. Since orbits are not in general edge-on, and will depend upon the orbital inclination, argument of perihelion, and longitude of the ascending node ( $\Omega$ ), we need to use the mapping,  $\cos(\alpha) = \sin(i) \cos(\theta + \omega_p)$  and rotate to the celestial frame. Using the Müller matrix for rotation through an angle  $\gamma$  to transform  $\mathbf{I}$  to the celestial frame, we obtain (Wiktorowicz 2009):

$$\begin{aligned} Q(\theta) &= Q'(\theta) \cos(2\gamma) - U'(\theta) \sin(2\gamma), \\ U(\theta) &= Q'(\theta) \sin(2\gamma) + U'(\theta) \cos(2\gamma), \end{aligned} \quad (11)$$

where  $\gamma = \Omega + 270^\circ$  and we have retained the possibility that  $U'(\theta) \neq 0$ . Note again that  $P(\theta) = \frac{\sqrt{(Q'(\theta)^2 + U'(\theta)^2)}}{I(\theta)}$ . Hence, with these equations we have the linear Stokes vector for arbitrary orbital elements.

### 3. ALBEDOS AND LIGHT CURVES OF GIANT EXOPLANETS: GENERAL EXPECTATIONS

In the optical, from  $\sim 0.4 \mu\text{m}$  to  $\sim 1.0 \mu\text{m}$ , a giant exoplanet is expected to have prominent methane features near  $0.62 \mu\text{m}$ ,  $0.74 \mu\text{m}$ ,  $0.81 \mu\text{m}$ , and  $0.89 \mu\text{m}$ , a broad water feature near  $\sim 0.94 \mu\text{m}$ , and ammonia bands at  $\sim 0.65 \mu\text{m}$  and  $\sim 0.79 \mu\text{m}$ . These planet/star flux ratios for distances from 1.0 AU to 10 AU and masses from  $0.5 M_J$  to  $8 M_J$  can vary from above  $10^{-7}$  to  $\sim 10^{-10}$ . The strengths in absorption bands and the continuum of the reflection and albedo spectra depend upon the atmospheric composition and molecular abundances; the temperature/pressure profile; the possible presence of water and ammonia clouds; and the presence, altitude, complex indices of refraction, and particle sizes of whatever aerosols and hazes may be present. The latter could be polyacetylenes, tholins (Sagan & Khare 1979; Khare et al. 1984), or various sulfur or phosphorus compounds. In general, gas-phase absorption opacities increase with temperature and metallicity, thereby decreasing the scattering albedo, and, hence, the geometric albedo. At the shortest wavelengths ( $\leq 0.5 \mu\text{m}$ ), Rayleigh scattering by gas (mostly  $\text{H}_2$ ) and scattering by haze/cloud particles can dominate, though  $A_g$  can still be modulated by methane features. At longer wavelengths, still shortward of  $\sim 1.0 \mu\text{m}$ , molecular absorption bands and clouds sculpt the albedo and reflection spectra. There is often a slight anti-correlation in the effects of clouds in the optical and infrared, with the optical fluxes increasing and the infrared fluxes decreasing with increasing cloud depth.

Water and ammonia clouds are expected in the atmospheres of most of the WFIRST targets. Generally, clouds significantly increase reflection albedos. Differences in the particle size distributions of the principal condensates can have large quantitative, or even qualitative, effects on the resulting albedo spectra. In general, larger particle sizes, and wider particle size distributions result in lower albedos. For such condensate clouds, their physical base should be at the ‘‘Clausius-Clapyron’’ condensation level, easily determined thermodynamically. Their geometric thicknesses are unknown, but are expected to be of order the local pressure scale height.

In the optical, at the wide separations relevant to

WFIRST/CGI, the planet/star flux ratio is determined almost entirely by reflected starlight off a giant’s atmosphere. However, such is not the case in the infrared, where thermally re-emitted radiation, can determine the ratio. This is particularly relevant for more massive and/or young exoplanet targets for WFIRST, for which the outward core flux can still be large and the planet/star flux ratios may be thermal longward of  $\sim 0.75\text{--}0.8 \mu\text{m}$ . Hence, although the optical spectrum is expected to be fully phase-dependent, this may not be the case in the near infrared, where emission may be more isotropic, depending upon the efficiency of advection of heat to the night side of the planet.

For instance, for Jupiter at 5.2 AU the nightside is as bright as the dayside in the infrared longward of one micron (with an effective temperature of  $\sim 125 \text{ K}$ ). This is in part a consequence of the shallowness of the radiative-convective boundary and the consequent direct heating by the stellar infrared of the convective zone itself. Such heat is efficiently redistributed around the planet by convection, equally to both day and night sides. This fact will be relevant for the WFIRST coronagraph targets. For close-in giants (i.e., transiting giant exoplanets not accessible to WFIRST), that interface is too deep to be directly heated, and as a consequence much of the stellar heat redistribution is done by zonal atmospheric flows that lose a large fraction of their extra heat before reaching the nightside. As a result, for them there are significant day/night thermal and spectral differences. Hence, the phase curves as a function of wavelength can be used to explore the stellar flux level or orbital distance at which the mechanism of day/night heat transport for giant planets transitions.

Though Jupiter and Saturn themselves are useful testbeds, it would be a mistake to extrapolate their albedo spectra to giant exoplanets as a whole. The population of the latter will be scattered in orbital distance, parent star, atmospheric composition, orbital eccentricity, planet mass, and planet age. All these characteristics, in particular orbital distance, mass, and age, can result in large, qualitative variations in albedo spectra among the class of giant exoplanets in the wide orbits that can be studied by WFIRST/CGI. For instance, the optical and geometrical thicknesses of clouds will vary with planet gravity. Their positions in pressure space and the atmospheric temperature/pressure profiles (that strongly influence the gas-phase molecular scattering albedos) will be functions of incident stellar flux, itself a function of orbital distance. All these effects could translate into changes in albedo spectra of factors of a few.

The fluxes from  $0.4 \mu\text{m}$  to  $0.65 \mu\text{m}$  in the optical from irradiated, yet cloud-free, brown dwarfs can be enhanced by Rayleigh reflection by as much as a factor of 10 over those from isolated brown dwarfs. This is particularly true of old or low-mass brown dwarfs and is a predictable function of distance (Burrows et al. 2004).

In this section, we rely heavily on the theory of giant planet albedos and light curves created by Sudarsky et al. (2000, 2003, 2005) and Burrows et al. (2004). The models generated in this sequence of papers provided a useful, detailed set of theoretical models as a function of mass, age, orbital distance, and cloud properties that can frame current discussions and inform future models

and retrievals.

Those heritage models used an atmosphere code that placed water and/or ammonia clouds at pressure levels determined in a fully iterative, converged fashion. They used the Cooper et al. (2003) theory to determine modal particle sizes, and the Deirmendjian (1964,1969) particle size distribution. The modal particle size was found to be very roughly constant with age, but steeply decreasing with increasing surface gravity (and, hence, planet mass), and was assumed not to vary with altitude. The bases of the clouds were put at the intersection of the corresponding condensation curve with the planet’s temperature/pressure profile. The scale height of a cloud was assumed to be equal to one pressure scale height. For the ammonia clouds that form in the orbital distance sequence from 0.2 to 15 AU (i.e., at  $\gtrsim 4.5$  AU), those calculations derived modal particle sizes that hovered near  $50\text{--}60\text{ }\mu\text{m}$ . The corresponding particle sizes in the water clouds were near  $110\text{ }\mu\text{m}$ . Little weight should be given to these estimates, which future data should better constrain. The irradiating stellar spectra were taken from Kurucz (1994) and the inner atmosphere boundary conditions were taken from the evolutionary models of Burrows et al. (1997). Equilibrium molecular and atomic compositions and abundances were obtained from Burrows & Sharp (1999) and the gas-phase opacities employed were eventually published in Sharp & Burrows (2007). Mie theory was used to obtain the absorptive and scattering opacities of the cloud particles.

When not plotted as a function of orbital phase, the planet/star flux ratios plotted below are “phase-averaged.” By phase-averaged we mean that flux, when integrated over wavelength, would equal the incident stellar power on the planet, plus the internal luminosity of the cooling core. As described in Sudarsky, Burrows, & Hubeny (2003), phase-averaging is thus a normalization that ensures energy conservation and is the average flux seen at Earth over a full orbital traverse. Hence, the maximum planet/star flux would always be larger than this average.

### 3.1. Semi-Major-Axis/Orbital Distance Dependence

Figure 3 depicts the resulting temperature-pressure ( $T/P$ ) profiles for a  $1\text{-}M_J$ ,  $5\text{-Gyr}$  giant exoplanet orbiting a G2V star at a range of distances from 0.2 AU to 15 AU. The distance determines the irradiating flux, which in turn, along with the interior flux, establishes the  $T/P$  profile. Also shown are the condensation curves for water and ammonia clouds. When appropriate, and as discussed above, water and ammonia clouds are included in the models. Note that water clouds form around a G2V star exterior to a distance near 1.5 AU, whereas ammonia clouds form around such a star exterior to a distance near 4.5 AU. Consistent with these systematics, Jupiter itself, with a dominant ammonia cloud layer, is at the distance from the Sun of  $\sim 5.2$  AU. Not shown on this figure, but a product of this study, Burrows et al. (2004) found that at this orbital distance and as early as  $\sim 50$  Myr, water clouds form in Jovian-mass objects. Note also that at 4 AU, even after 5 Gyr, ammonia clouds have not yet formed in the atmosphere of an irradiated  $1\text{-}M_J$  giant exoplanet. This is not true for a similar object in isolation (Burrows, Sudarsky, & Lunine 2003).

Since the atmospheric temperatures vary with stellar

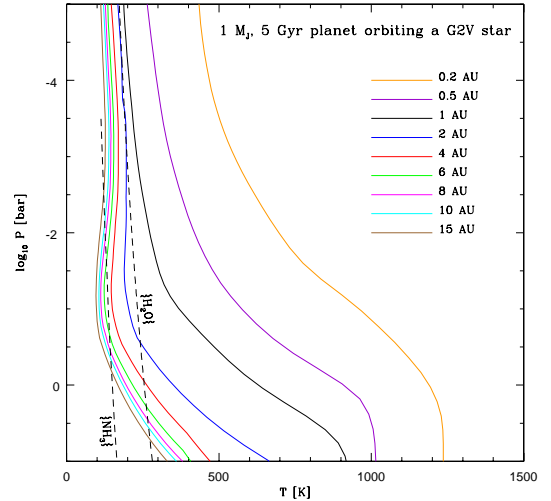


FIG. 3.— Profiles of atmospheric temperature (in Kelvin) versus the logarithm base ten of the pressure (in bars) for a family of irradiated  $1\text{-}M_J$  giant exoplanets around a G2V star as a function of orbital distance. Note that the pressure is decreasing along the ordinate, which thereby resembles altitude. The orbits are assumed to be circular, the planets are assumed to have a radius of  $1.0\text{ }R_J$ , the effective temperature of the inner boundary flux is set equal to 100 K, and the orbital separations vary from 0.2 AU to 15 AU. The intercepts with the dashed lines identified with either  $\{\text{NH}_3\}$  or  $\{\text{H}_2\text{O}\}$  denote the positions where the corresponding clouds form. Figure taken from Burrows et al. (2004).

distance, because such variation determines whether water or ammonia clouds form, the albedos will vary significantly with orbital distance. In fact, one expects the albedo spectrum of a giant planet to depend sensitively upon orbital distance, mass, age, and parent star. Figure 4 depicts the geometric albedo spectra of a  $1\text{-}M_J$ ,  $5\text{-Gyr}$  exoplanet at the various orbital distances used in Figure 3. Also shown are the positions of the prominent molecular bands of methane and water. The presence of clouds profoundly affects the reflectivity of the planet. Figure 4 demonstrates that the closest, being hotter and clearer, have low albedos, while the furthest, being cooler and having either water clouds ( $\leq 300$  K; generally  $a \geq 1.5$  AU) or ammonia clouds ( $\leq 160$  K; generally  $a \geq 4.0$  AU), have higher albedos. The optical albedo rises significantly with increasing orbital radius between  $\sim 0.2$  AU and 1 AU, even though there are no water clouds present. With the onset of water clouds, the optical albedo rises further still, which is seen clearly in the model at 2 AU. The onset and thickening of reflective ammonia clouds at larger orbital distances results in the highest albedos at most optical and near-infrared wavelengths. For greater distances than  $\sim 1.0$  AU, in these models the presence of water clouds slightly mutes the variation with wavelength in the planetary spectra. Hence, smoothed water features and methane bands predominate beyond  $\sim 1.5$  AU. Note that because the methane abundances and cloud presence and properties are functions of temperature, the albedo spectrum is a non-monotonic function of planet mass and age (which determine in part the degree to which the planet has cooled), orbital distance, stellar type, and planet elemental composition. Moreover, as Figure 5 demonstrates, the planet/star flux ratio does not follow an inverse-square law with orbital distance, and the deviations from such behavior are functions of wavelength. Hence, giant planet reflectivity is a



rich function of planet/orbital properties and its optical spectrum can in principle elucidate the planet's atmosphere and history. Figure 6 provides some of the phase-averaged planet/star flux ratios from  $\sim 0.4 \mu\text{m}$  to  $\sim 1.0 \mu\text{m}$  that correspond to the models in Figures 3 and 4.

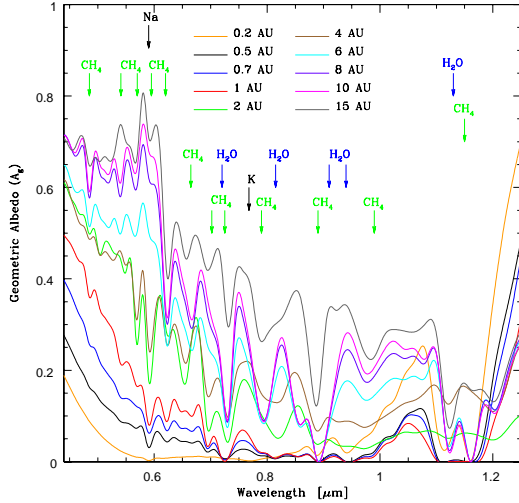


FIG. 4.— Low-resolution, wavelength-dependent geometric albedos of  $1\text{-}M_J$ , 5 Gyr giant exoplanets ranging in orbital distance from 0.2 AU to 15 AU about a G2V star as a function of wavelength from 0.4 to  $1.25 \mu\text{m}$ . WFIRST extends only to  $\sim 1.0 \mu\text{m}$ . Superposed are the positions of the methane and water features in this wavelength range. The models have been deresolved to  $R = 100$ . Possible reddening effects of photochemical hazes are not incorporated. Figure taken from Burrows et al. (2004).

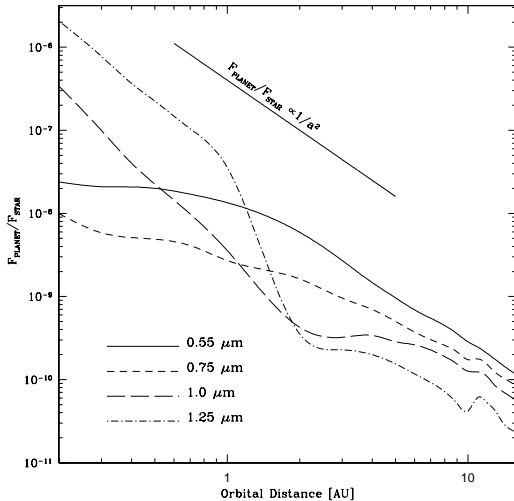


FIG. 5.— Planet/star flux ratio as a function of orbital distance at  $0.55 \mu\text{m}$ ,  $0.75 \mu\text{m}$ ,  $1 \mu\text{m}$ , and  $1.25 \mu\text{m}$  assuming a G2V central star, taken from Sudarsky et al. (2005). In each case, the plotted value corresponds to a planet at greatest elongation with an orbital inclination of  $80^\circ$ . Note that the planet/star flux ratios do not follow a simple  $1/a^2$  law.

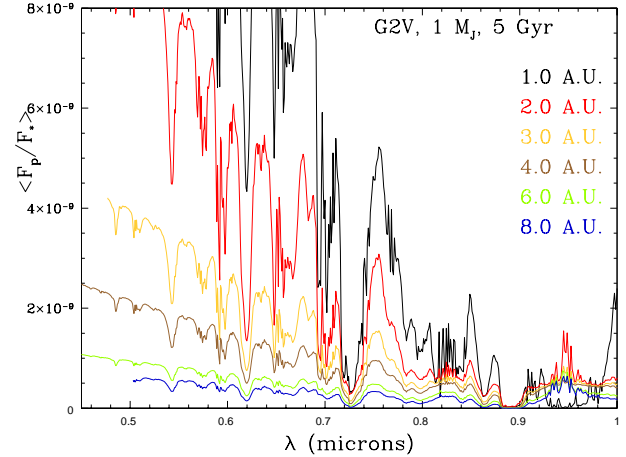


FIG. 6.— Phase-averaged planet/star flux ratios in the optical ( $0.45$  to  $1.0 \mu\text{m}$ ) for a  $1\text{-}M_J$  giant planet orbiting a G2 V star as a function of orbital distance (semi-major axis) from 1.0 to 8.0 AU. The model data were taken from Burrows et al. (2004). Note that some models seem to show emission, some absorption, at the water feature near  $0.94 \mu\text{m}$ . See text for a discussion. These models employ the geometric albedos shown in Figure 4, but include a thermal component due to the residual cooling of the planet core (Burrows et al. 1997).

Figures 7 and 8 incorporate phase functions ( $\Phi(\alpha)$ ) calculated by Sudarsky et al. (2005) and Burrows et al. (2004) and convey representative theoretical phase dependences/light curves for semi-major axes of 6, 10, and 15 AU and of 1, 2, and 4 AU, respectively, at  $0.55 \mu\text{m}$ ,  $0.75 \mu\text{m}$ , and  $1.0 \mu\text{m}$ . An orbital inclination of  $80^\circ$  is assumed. These figures also provide the maximum planet/star ratios at greatest elongation (its maximum angular separation as seen from Earth). Given a stellar distance and an inner working angle (IWA  $\sim 0.1\text{--}0.2''$ ), Figures 7 and 8 can be used to compare with the expected contrast ratio performance of WFIRST/CGI to determine detectability as a function of phase and orbit. As these figures indicate, WFIRST should have sensitivity to a wide range of  $1\text{-}M_J$  giant exoplanets orbiting a solar-like star out to tens of parsecs.

As stated in Sudarsky et al. (2005), at  $0.55 \mu\text{m}$  and  $0.75 \mu\text{m}$ , the planet/star flux ratio near full phase is 3 to 4 times its value at greatest elongation. Hence, at these wavelengths, the planet/star flux ratios are not very different from those that would arise if we were to assume a Lambert phase function, in which case the ratio at full phase would be  $\pi$  times larger than at greatest elongation. However, at other phase angles and other wavelengths, model phase functions frequently differ by a wider margin from the Lambert phase function.

To gauge the dependence of the planet/star flux ratios on the cloud particle size assumed, Figures 9 and 10 (taken from Sudarsky et al. 2005) explore this dependence for water clouds in a  $1\text{-}M_J$  model at 2 AU from a G2V star at two different wavelengths. Also shown is the corresponding cloud-free model<sup>4</sup>. At both  $0.55 \mu\text{m}$  and  $0.75 \mu\text{m}$ , the  $1 \mu\text{m}$  particle size models exhibit higher

<sup>4</sup> Recall that the models presented via Figures 3, 4, and 6 employed the model of Cooper et al. (2003) to obtain the modal particle size, and that for a water cloud such particle sizes varied around  $\sim 100 \mu\text{m}$ .

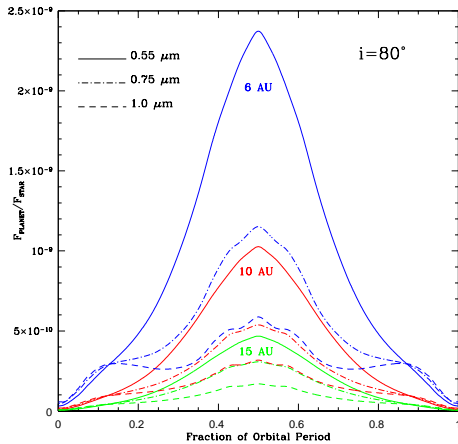


FIG. 7.— Light curves at 0.55  $\mu\text{m}$ , 0.75  $\mu\text{m}$ , and 1  $\mu\text{m}$  for 1- $M_J$  giant exoplanets in circular orbits inclined to  $80^\circ$  at distances of 6 AU, 10 AU, and 15 AU from a G2V star. The planet/star flux ratio is plotted. Each of these models contains an ammonia ice cloud layer above a deeper water cloud deck. Taken from Burrows et al. (2004) and Sudarsky et al. (2005).

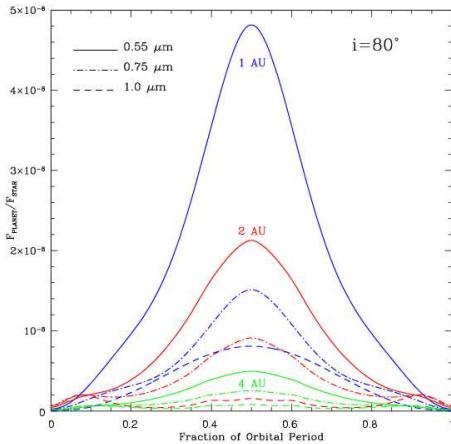


FIG. 8.— Light curves at 0.55, 0.75, and 1.0 microns for model gas giants in circular orbits inclined to 80 degrees at distances of 1 AU, 2 AU, and 4 AU from a G2V star. The planet/star flux ratio is plotted. The models at 2 AU and 4 AU contain water ice clouds in their upper atmospheres, while the 1 AU model does not. Taken from Burrows et al. (2004) and Sudarsky et al. (2005).

planet/star flux ratios and smoother light curves than for those models with larger particles. At 0.55  $\mu\text{m}$ , the planet/star flux ratios do not vary substantially over a range of modal particle sizes from 3 to 100  $\mu\text{m}$  (although the shapes of the light curves differ somewhat). This result contrasts with those of the same giant at 0.75  $\mu\text{m}$ , where the planet/star flux ratio becomes progressively lower with increasing particle size. Such results indicate the importance not only of condensate particle size, but of wavelength-dependent light curves.

### 3.2. Mass and Age Dependence

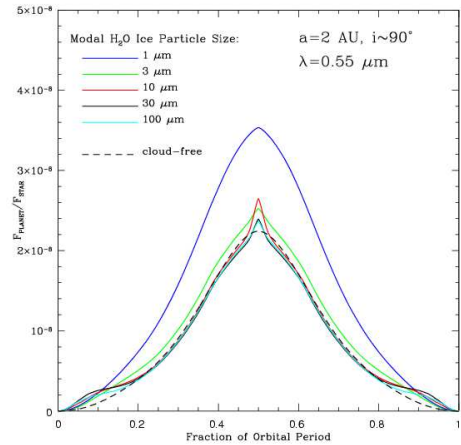


FIG. 9.— The dependence of the planet/star flux ratio on condensate particle size at a wavelength of 0.55 microns. Model light curves for EGPs at 2 AU with modal  $\text{H}_2\text{O}$  ice particle sizes of 1, 3, 10, 30, and 100 microns are depicted. Shown for comparison is a cloud-free model (black dashed curve). In order to show the full variation in the shapes and magnitudes of the light curves with particle size, we have set the orbital inclination to approximately 90 degrees so that the opposition effect, present for many of the models, can be seen in full. Transit effects are not modeled. Figure taken from Sudarsky et al. (2005).

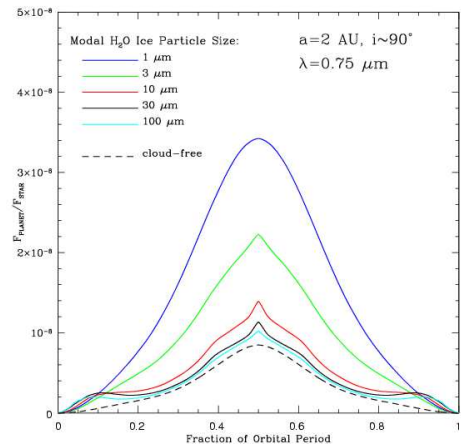


FIG. 10.— Same as in Figure 9, but for 0.75  $\mu\text{m}$ .

Figure 11 shows the predicted planet/star phase-averaged contrast ratio spectrum for giant planet masses from 0.5 to 8.0  $M_J$  at an age of 5 Gyr and at an orbital distance of 3 AU. Older giant exoplanets have progressively deeper water clouds. These older clouds are also thicker (have higher column depths). This results in a slightly increasing reflected optical flux with increasing age. Conversely, larger-mass giants have higher surface gravities, which result in water clouds with lower column depths, and, hence, lower optical depths, despite the possible contrary trend of modal particle size. Therefore, as seen in Figure 11, at a given age and at the shorter optical wavelengths, higher-mass giant exoplanets have slightly smaller planet/star flux ratios. However, also at a given age, higher mass giant planets have higher  $T_{\text{eff}}$  and internal luminosities. This is due to the higher core fluxes of more massive planets that are still cooling from formation. Therefore, at longer wavelengths (greater than

or equal to  $\sim 0.8 \mu\text{m}$ ) still accessible to WFIRST/CGI, the flux ratios at a given age are higher for more massive giants. For such planets younger than 5 Gyr, the effect can be larger still. Therefore, for more massive giant planets and brown dwarfs, and for their younger cohort, the flux ratios longward of  $0.7\text{--}0.8 \mu\text{m}$  can be much higher than for an old,  $1\text{-}M_{\text{J}}$  giant such as Jupiter. This also means that the planet/star flux ratios at these longer wavelengths for the more massive and/or younger exoplanets will be weaker functions of orbital phase and their apparent albedos can be greater than one. For such giant exoplanets, extrapolations from Jupiter should be wildly in error.

Around  $0.94 \mu\text{m}$ , as seen in Figure 11, some of the models show flux enhancements, while others show the flux deficits one would expect due to band absorption. This is due in part to a combination of the dependence of the water absorption opacity on temperature and on metallicity. All else being equal, the higher the metallicity or the higher the temperature the lower the water band peak in the albedo spectrum. Condensation of gaseous water at lower atmospheric temperatures will also affect the gas-phase water absorption opacity. All these effects alter the scattering albedo in this wavelength band, and hence, the associated geometric albedo. The magnitude of this effect will depend upon details, but its presence could constrain 1) metallicity and 2) water temperature and condensation. Hence, the  $0.94\text{-}\mu\text{m}$  water band is expected to be a diagnostic of metallicity (or elemental composition), orbital distance, and mass.

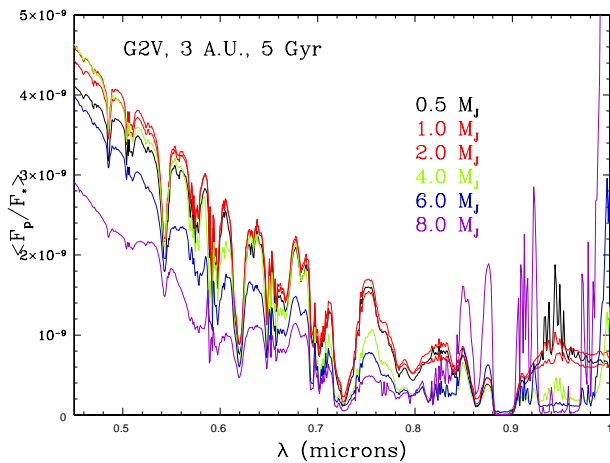


FIG. 11.— Phase-averaged planet/star flux ratios in the optical as a function of giant planet mass (in  $M_{\text{J}}$ ) at 3 AU from a 5 Gyr-year-old G2 V star. Higher gravity generally leads to lower fluxes at short wavelengths. Note that for these mass/age combinations, the more massive planets ( $6.0$  and  $8.0 M_{\text{J}}$ ) have enhanced fluxes longward of  $\sim 0.8 \mu\text{m}$ , due to a competitive contribution of thermal emission powered by their greater residual heat of formation (Burrows et al. 1997). This variety highlights the diagnostic potential of even low-resolution optical spectra and spectrophotometry to constrain various giant planet properties.

### 3.3. Predictions for Known Radial-Velocity Giant Exoplanets

One set of useful and reliable targets for a WFIRST exoplanet campaign will be nearby known RV planets at wide separations. There are perhaps  $\sim 20\text{--}30$  of these, and they include 55 Cnc d (IWA(max) =  $0.44''$ ), 47 UMa c (IWA(max) =  $0.28''$ ), 47 UMa b (IWA(max) =  $0.16''$ ), Gl 777Ab (IWA(max) =  $0.23''$ ), HD 39091b (IWA(max) =  $0.16''$ ), 14 Her b (IWA(max) =  $0.15''$ ), and  $\nu$  And d (IWA(max) =  $0.19''$ ). Table 1 lists some of these planets and some of their relevant characteristics. Phase-averaged planet/star ratios versus wavelength for this target class are shown in the left panel of Figure 12. As these figures demonstrate, the flux ratios in the optical for these planets are in principle accessible to WFIRST and vary substantially from object to object. We note that the high mass of HD 39091b elevates its likely flux ratio longward of  $\sim 0.75 \mu\text{m}$  by an order of magnitude or more, bearing out the point made about younger and more massive exoplanets at longer wavelengths made in §3.2.

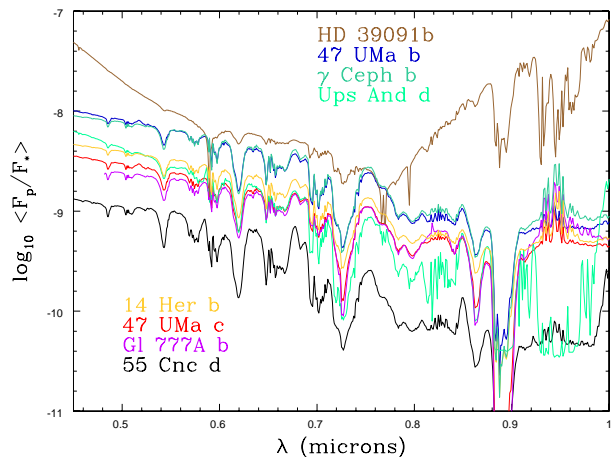


FIG. 12.— Phase-averaged planet/star flux ratios in the optical for representative non-transiting radial-velocity exoplanets with planet-star angular separations accessible to WFIRST/CGI at greatest elongation. These include 55 Cnc d ( $0.44''$ ), 47 UMa c ( $0.28''$ ), 47 UMa b ( $0.16''$ ),  $\Upsilon$  And d ( $0.19''$ ), Gl 777A b ( $0.23''$ ), HD 39091b ( $0.16''$ ), 14 Her b ( $0.15''$ ), and  $\gamma$  Ceph b ( $0.15''$ ). The angles in parentheses are the ratios of semi-major axis to Earth-star distance. These models are taken from Burrows et al. (2004). Notice that some of the models have local peaks (e.g., for  $\gamma$  Ceph b), some local troughs (e.g., for  $\Upsilon$  And b), in a  $0.94 \mu\text{m}$  water feature. This can be indicative of the presence or absence of gaseous water in abundance and of the atmospheric temperature (which affects the corresponding absorption opacity and scattering albedo,  $\omega$ ). Also, as the model for HD 39091b indicates, massive giant planets will retain their heat of formation and emit copiously in the  $0.7\text{--}1.0 \mu\text{m}$  band, far more than they reflect. Hence, this spectral region is a good mass/age index of the orbiting giant. As this plot demonstrates,  $F_p/F_*$  is not merely a scaled one-parameter family of passive and uniform reflection spectra, but has many diagnostic band ratios and/or colors in the optical.

### 3.4. Inclination and Eccentricity Dependence

The interpretation of optical reflection spectra is complicated by the need to factor in the effects of orbital inclination, eccentricity, and argument of periape — planet



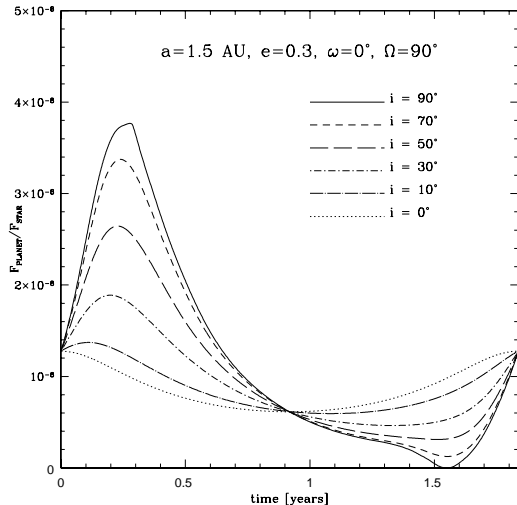


FIG. 13.— Variation with inclination of the optical light curve for an elliptical orbit (G2V central star,  $a = 1.5$  AU,  $e = 0.3$ ). For a highly-inclined orbit, the peak of the planet/star flux ratio is a factor of  $\sim 3$  greater than for a face-on ( $i = 0$  degrees) orbit. The (symmetric) variation for the face-on case is due entirely to the variation in the planet-star distance over an eccentric orbit. Taken from Sudarsky et al. (2005).

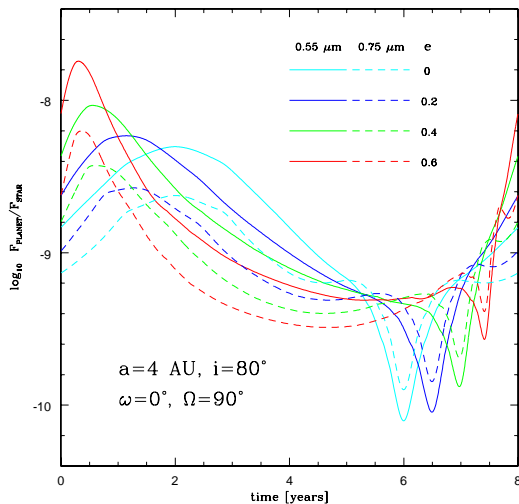


FIG. 14.— The optical planet/star flux ratio as a function of eccentricity for a cloud-free 1- $M_J$  giant planet at 1 AU, fixing  $i$  at  $90^\circ$  and  $\omega_p$  at  $0^\circ$ . Only for  $e=0$  does the peak of the light curve coincide with full phase. Taken from Sudarsky et al. (2005).

orbits will not in general be circular and edge-on. In addition, the planets will not always be at greatest elongation. In principle, the Keplerian elements can be determined independently from RV data, when available, but can also be derived astrometrically from multi-epoch WFIRST observations themselves. Since *Gaia* astrometry on the observed systems will be public by the time WFIRST is operational, that source of orbital information could be invaluable. Be that as it may, as stated, most planets observed by the WFIRST coronagraph will not be in simple, edge-on, circular orbits and the correc-

tions, though straightforward theoretically, are not small. We recall that Figure 2 provided some model phase functions and noted that at a given phase or mean anomaly  $\Phi(\alpha)$  can range by factors of two or more. Moreover, the Lambert phase function frequently used can be significantly in error. Despite this, the phase variation of the intensity should be a smooth function of orbital phase, while we expect that the variation of the planet's polarization and polarization angle could be much less smooth. Fluri & Berdyugnia (2010) suggest, and experience with Venus demonstrates (Hansen & Hovenier 1974), that polarization as a function of phase (and wavelength) can be used to constrain not only cloud properties, but orbital elements as well (§5).

Figure 13 depicts an example of planet/star flux ratio variation with orbital inclination (for an eccentric orbit), and Figure 14 depicts sample variations with eccentricity. Clearly, large variations in flux ratio along an orbital traverse are possible and need to be incorporated into the modeling, particularly of the absolute flux levels. What these figures show is 1) that the flux ratios anticipated are indeed within WFIRST's coronagraphic reach, and 2) that the dependence upon Keplerian elements must be incorporated into the analysis.

#### 4. JUPITER'S ALBEDO SPECTRUM

Even if present in trace amounts, stratospheric hazes and tropospheric “chromophores” (West et al. 1986; Pope et al. 1992) can alter emergent reflection spectra substantially, particularly in the ultraviolet and blue regions of the spectrum. Karkoschka (1994,1998) has obtained full-disk geometric albedo spectra of Jupiter, Saturn, Uranus, and Neptune. Figure 15 portrays these optical albedo spectra, which show that the atmospheres of Jupiter and Saturn, but not of Uranus and Neptune, indeed contain a trace species well-mixed in their upper ammonia cloud decks that is depressing the reflected flux shortward of  $\sim 0.6 \mu\text{m}$  from what one would expect from the increase with frequency of the Rayleigh and ammonia cloud scattering cross sections (§3). It is this trace species, with a mixing ratio of perhaps no more than  $10^{-9}$ – $10^{-8}$ , that gives Jupiter and Saturn their reddish hues, and it is its absence in Uranus and Neptune that maintains their expected bluish tinge. The optical albedo spectra longward of  $\sim 0.6 \mu\text{m}$  of these four solar-system planets are otherwise as expected, given the systematics described in §3, and are dominated by methane absorption features and ammonia clouds.

Figure 16 depicts two model comparisons with Jupiter's measured albedo spectrum. Relying upon Mie scattering theory and choices for chromophore particle size distributions, tholin appears to reproduce the UV/blue region of the albedo better than  $P_4$ , but a number of other possible trace species are still in contention. Polyacetylenes (Rages 1997), tholins, sulfur compounds, or elemental phosphorus have been suggested, and UV photolytic chemistry may be involved.

Given this mixed picture, it is not known how prevalent this trace species may be among the giant exoplanets. As in the case of Uranus and Neptune, they may not be present generically. Be that as it may, libraries now exist for the complex indices of refraction of many potential chromophores, and these can be used, if necessary, to fit the anticipated data shortward of  $\sim 0.6 \mu\text{m}$ . Note that

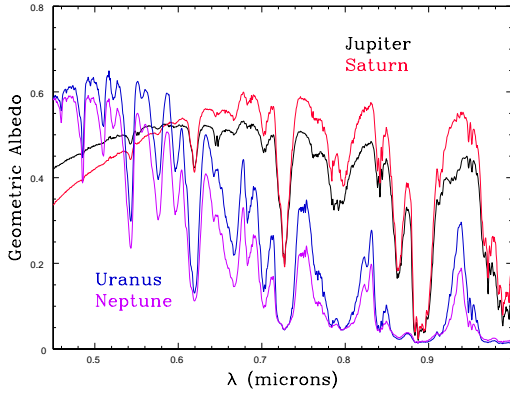


FIG. 15.— The geometric albedo spectra of Jupiter, Saturn, Uranus and Neptune, from Karkoschka 1994. Note the dominance of the methane bands, but also the differences between Jupiter and Saturn and Uranus and Neptune. The greater depths of the features for the “ice giants” are due to the greater column depths for the lower gravities and the higher methane abundances.

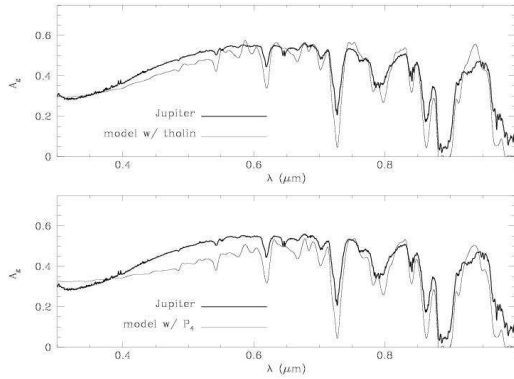


FIG. 16.— The full-disk geometric albedo spectrum of Jupiter (thick curve) from Karkoschka 1994, compared with model albedo spectra (thin curves). The top model utilizes tholin as a chromophore, while the bottom model uses P4. Models taken from Sudarsky et al. (2000).

the mere change of average albedo slope has information — correlations of the red or blue colors of WFIRST/CGI targets with stellar type and metallicity, planet mass, or orbital distance could teach us not only about giant exoplanets, but about the solar-system giants as well.

In any case, the properties of clouds and hazes will have to be parametrized when fitting the WFIRST/CGI albedo data. Physically, the cloud/haze position, abundance, modal particle size, and complex index of refraction as a function of wavelength are determinative. Practically, the position of the cloud top, the particle scattering albedo, particle number density, and wavelength dependence will have to be modeled. Since clouds and hazes introduce a continuum extinction spectrum, this can be modeled with only a few degrees of freedom. The indices of water and ammonia droplets are understood, and the positions of their cloud bases can be derived from their known condensation curves, but specific haze materials can be injected into the fits, or parametrized. We note that the various methane spectral features are formed at different heights and pressures

in the atmosphere, providing a means to break possible (quasi-)degeneracies and derive cloud and approximate molecular abundances separately. Hence, with the presence of clouds, but also of multiple bands, fitting multiple methane and water feature depths simultaneously should allow one to break the various degeneracies and derive physical abundances, gravities, and, perhaps, temperatures.

## 5. POLARIZATION

The exoplanet case for having a full linear Stokes capability on WFIRST/CGI is strong (Schmid et al. 2006). Estimates of peak exoplanet polarizations, with either Rayleigh or various Mie particles, range from 10% to 90% (Madhusudhan & Burrows 2011; Stam et al. 2004). The bottom panel of Figure 17 plots the magnitude of the polarization and its variation with orbital phase, as a function of particle scattering albedo ( $\omega$ ), due to vector Rayleigh scattering in a homogeneous atmosphere. Table 2 provides the geometric albedos, peak polarizations, and phase angle at peak for vector Rayleigh scattering, also as a function of  $\omega$ . For such an atmosphere, the peak polarization is always above 32.6%. Haze and cloud particles (as determined from Mie theory) are generally less polarizing than molecular Rayleigh scatterers, but are Rayleigh-like in the small particle ( $x = 2\pi a/\lambda \ll 1$ ) limit. This difference between the polarization for gas molecules and that for typical cloud and aerosol particles makes linear polarization a valuable tool for determining the presence and nature of those particles (Hansen & Travis 1974). This is all the more germane when we note that at shorter wavelengths, polarization generally contains information about the upper atmosphere, while at longer wavelengths clouds deeper in the atmosphere are probed. For example, if there is a Rayleigh scattering layer at depth, the more penetrating long-wavelength radiation can emerge more polarized than the short-wavelength radiation. Hence, a polarization color index (for example, ratioing blue with red or red with I-band) can reveal the presence, thickness, and optical depth of a Rayleigh scattering layer (Buenzli & Schmid 2009). Moreover, the total intensity generally decreases with increasing orbital phase angle from 0 to 90°, while the percent polarization generally increases in this interval. This results in a phase angle at which the polarized flux (as opposed to the polarized fraction) is a maximum. For conservative Rayleigh scattering, this angle is  $\sim 65^\circ$ , but it is generally larger for haze particles. Hence, this angle alone can be used as a diagnostic of the presence of aerosols (Buenzli & Schmid 2009).

Importantly, multiple scattering does not smooth out angular features in the polarization (i.e.,  $Q$ ), as it does in the light curve intensities (i.e.,  $I$ ). Those features bespeak particle refractive indices and sizes. Indeed, Stam et al (2004) note that planetary polarization at a given wavelength may be a more diagnostic function of phase than the light curve (i.e.,  $\Phi(\alpha)$ ) in probing the cloud and haze structures and positions in gas giant atmospheres. They emphasize the relative nature of a polarization measure (hence, its intrinsically more accurate character) and conclude that the degree of polarization in both spectral bands and the continuum depends strongly upon atmospheric composition and structure. More powerfully, when combining geometric albedo and

polarization data as a function of wavelength simultaneously (for a known orbital phase), one is able to break various approximate degeneracies introduced by the presence of clouds/hazes. Figure 18 from Stam et al. (2009) depicts both a scaled flux (left) and the degree of polarization (right) as a function of wavelength in the optical for three different atmosphere models at quadrature. For all models, the methane spectral features are prominent, and for the cloudy models the fluxes are larger than for the pure Rayleigh scattering model. At the same time, the polarizations for the cloudy models are smaller, and have the opposite dependence upon wavelength, particularly in the continuum. Moreover, the tropospheric and stratospheric cloud models can be distinguished by the line to continuum polarization ratios. Finally, though the fractional polarization can be large in strong absorption bands, while the flux itself is small (due to the absorption), the continuum does not suffer from this effect. Hence, both flux and polarization ratio indices between the absorption bands and the continuum are useful diagnostics of scattering cloud depth, the presence of aerosols, particle size and make-up, and the relative contribution of Rayleigh scattering.

Fluri & Berdyugina (2010) have suggested, if a reasonable partial phase curve can be obtained, that Keplerian orbital elements of an exoplanet such as inclination, eccentricity, and the position angle of the ascending node can be constrained using polarization measurements as a function of orbital phase or mean/true anomaly. The peak polarization at a given wavelength is independent of orbital inclination and reflects the presence and layering of hazes and clouds, but the polarization phase curve can constrain orbital elements such as inclination particularly well (§2.2). We note, however, that *Gaia* astrometry may have already provided the orbital elements of many of the WFIRST exoplanet targets prior to the latter’s launch, in which case the orbital information extracted from the rotation of the direction of polarization with phase would be, however useful, merely confirmatory. In fact, the likely availability of planet orbital data from *Gaia* will make interpreting both intensity and polarization data much less ambiguous for single-epoch observations by providing the planet’s Keplerian elements. Knowledge of the orbit would usefully reduce the number of free parameters to be deduced.

As Hansen & Hovenier (1971) have articulated, the sharpness of the angular variations in the polarization increases markedly for larger particles or shorter wavelengths (larger  $x = 2\pi a/\lambda$ ), and this can be used to directly constrain particle size. In addition, if there are multiple particle species, each particle type contributes to the polarization approximately according to its share of the “single” scattered light (Hansen & Hovenier 1974). The robustness of the qualitative single-scattering result in the context even of multiple scattering leaves open the possibility that spherical droplets could imprint rainbow and/or glory effects. Interestingly, rainbow angles were seen in the polarization measurements of Venus. These measurements from  $0.365\ \mu\text{m}$  to  $0.99\ \mu\text{m}$  as a function of Venus’ orbital phase revealed a mean droplet size of  $1.05\ \mu\text{m}$  (with a  $\sim 7\%$  logarithmic spread), with a real part of the index of refraction from 1.46 to 1.43 for wavelengths from  $0.365$  to  $0.99\ \mu\text{m}$  (Hansen & Hovenier 1974). The latter cinched the composition of its clouds to be

sulfuric acid. The polarization for Venus at  $0.55\ \mu\text{m}$  is  $\sim 5\%$  and the Rayleigh fraction was determined to be  $\sim 4.5\%$ . Multi-band optical polarization measurements constrained Venus’ cloud modal particle size to better than  $10\%$ , and the real part of the index of refraction to  $\sim 1\%$ .

In addition, as measured by Pioneer 11 (Tomasko & Smith 1982) and Voyager 2 (West et al. 1983) at quadrature, the fractional polarization of the hazy moon Titan is near  $\sim 50\%$  from the R band to the near UV. Such a large polarization confirmed the small size of the aerosol particles in Titan’s upper atmosphere, but the concomitant large forward scattering inferred as a function of phase angle (Rages, Pollack, & Smith 1983) suggested that the haze particles could not be spherical (West & Smith 1991). Hence, light curve and polarization data together revealed quite a bit about the physical character of the particles in Titan’s haze layer. However, despite the inherent usefulness of polarization measurements as a function of wavelength and phase, few polarization measurements have been made of the outer-solar-system giants. Exceptions are the Pioneer 10 and 11 photopolarimetry measurements in the red and blue of Jupiter and Saturn (Smith & Tomasko 1984). These measurements were, however, angularly resolved and not full-disk. One reason for such sketchy full-disk coverage is that the two polarization channels on Voyager 1 failed after launch, depriving science of such useful data. Another is that the phase angles of Jupiter and Saturn at Earth are a paltry  $\sim 11^\circ$  and  $\sim 6^\circ$ , respectively. A third is the priority placed by planetary scientists on in-situ composition, charged-particle, and magnetic-field probes. However, since such in-situ measurements are not possible for exoplanets and the entire focus of exoplanet research is on remote sensing, a polarization capability should seem compelling. Hence, there is a strong case for full-linear Stokes imaging polarimetry on WFIRST-AFTA/CGI in support for its exoplanet campaign. Given that polarization filters may be deemed an important design feature for the WFIRST coronagraph, this could be a fortuitous alignment of circumstances.

We note that for the more massive (such as HD 39091b) and younger giant planets that may be WFIRST/CGI targets, their atmospheric temperatures may be high enough that the thermal component of the fluxes at the longer wavelengths in the WFIRST/CGI optical range may dominate the reflected component (§3; §3.2). This will mute the polarization fraction at these wavelengths, as well as the overall phase dependence of the corresponding planet/star flux ratios. When measured, this effect, a function of wavelength and identifiable in the phase dependence of both the intensity and the polarization fraction, could therefore be a useful diagnostic of both the planet’s thermal evolution and atmospheric temperature.

## 6. WFIRST/CGI SYNERGIES WITH OTHER HIGH-CONTRAST PLATFORMS

However, as discussed in §1, high-contrast imaging of giant exoplanets in the infrared is finally emerging to complement other methods of exoplanet discovery and characterization (Oppenheimer & Hinkley 2009). Moreover, super-Neptunes around M dwarfs might soon be within reach. Collectively, these direct-imaging in-

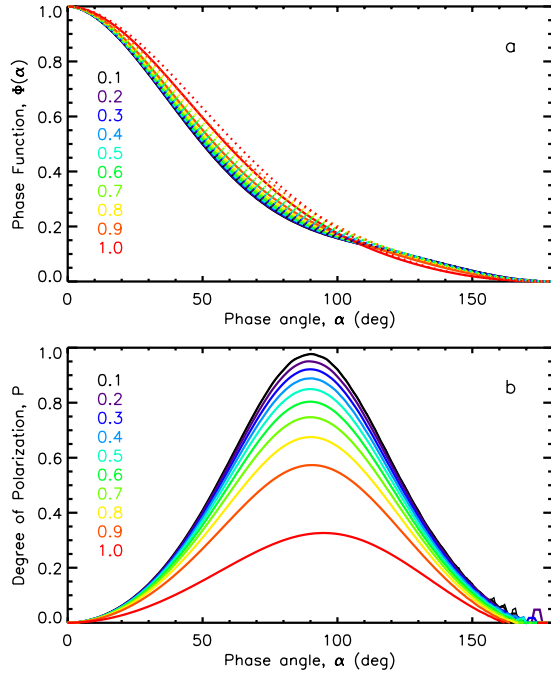


FIG. 17.— The various phase functions for a vector Rayleigh-scattering atmosphere (top), and the corresponding linear polarizations (bottom) as a function of orbital phase and scattering albedo ( $\omega$ , column of numbers) (from Madhusudhan & Burrows 2011).

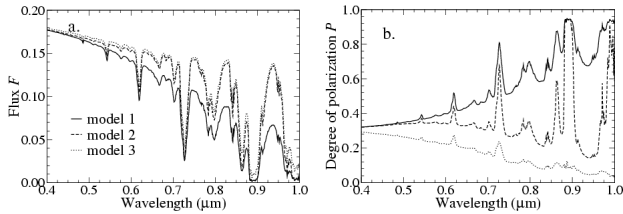


FIG. 18.— Multi-wavelength optical polarimetry measurements can constrain the atmospheric properties of giant exoplanets. The flux (left, in arbitrary units) and degree of polarization (right) of starlight reflected by three Jupiter-like gas giants for  $\alpha = 90^\circ$ . Planetary model atmosphere 1 (solid lines) contains only molecules, model 2 (dashed lines) is similar to model 1, except for a tropospheric cloud layer, and model 3 (dotted lines) is similar to model 2, except for a stratospheric haze layer. Figure taken from Stam et al. (2004).

struments will constitute significant improvements over *Spitzer* and what is currently possible in the mid-IR. For instance, GPI and SPHERE will have greater planet/star sensitivities ( $\sim 10^{-6} - 10^{-7}$ ) and smaller IWAs near  $\sim 0.1''$ , but are optimized in the H and K bands ( $\sim 1.6 \mu\text{m}$  and  $\sim 2.2 \mu\text{m}$ ). ELTs (such as E-ELT/EPICS and TMT/PFI) have the potential to achieve contrast ratios of  $\sim 10^{-8}$  in the H band and IWAs in the  $0.02''$  range. The H band has water and  $\text{CH}_4$  features, but such limited spectral coverage will put a premium on access to other bands.

However, there are as yet no optical data for planets such as HR 8799bcde,  $\beta$ -Pictoris, GQ Lup b, 2MASS 1207b, or GJ 504b. Expected planet/star contrast ratios in the optical for such planets range from  $10^{-8}$  to  $10^{-6}$ , well within the reach of WFIRST/CGI. More curi-

ously, other than WFIRST/CGI, there are no credible high-contrast campaigns or capabilities being planned or designed for exoplanet characterization in the optical. As Figure 1 demonstrates, the potential for WFIRST/CGI to fill this gap is tremendous. With their wide-angle separation, massive planets/brown dwarfs such as HR 8799bcde and their ilk will be low-lying fruit for WFIRST/CGI, yet are examples of planets and planetary systems for which optical data can be tightly constraining. Being self-luminous, massive exoplanet optical/infrared colors will determine temperatures. For the highest temperature targets, such as the HR 8799 planets with  $T_{\text{eff}} \sim 1000 \text{ K}$ , the Na D doublet at  $\sim 0.589 \mu\text{m}$  and the K I resonance doublet at  $\sim 0.77 \mu\text{m}$  should be easily identified with the WFIRST imager (by measuring the adjacent continuum and the lines, i.e. in and out of these absorption features), and the low-resolution integral-field spectrograph should clearly measure and trace the wide K I doublet. At lower  $T_{\text{eff}}$ s, the water feature at  $\sim 0.94 \mu\text{m}$  and the various methane features should easily be identifiable. In fact, comparing the optical spectra and photometric fluxes for both reflected-light and self-luminous targets would provide a unique window on the differences between giant planets over the very wide range of atmospheric thermal and compositional classes anticipated.

Moreover, an interesting synergy can be achieved by combining measurements using both WFIRST/CGI and JWST. WFIRST can provide data in the optical, while JWST will provide data both in the near- and the mid-infrared. There is a strong flux peak in the M band from  $\sim 4.0$  to  $5.5 \mu\text{m}$  to which JWST/NIRCam is sensitive. At an IWA of  $\sim 0.7''$ , the coronagraph on NIRCam is expected to have a planet/star contrast sensitivity near or below  $\sim 10^{-6}$  at  $\sim 4.5 \mu\text{m}$  and will cover the important spectral region from  $\sim 3.5 \mu\text{m}$  to  $\sim 5.0 \mu\text{m}$  where there are CO, water, and  $\text{CO}_2$  features in giant exoplanet spectra (Burrows, Sudarsky, & Lunine 2003). At smaller angles, its performance is likely to be significantly worse, but could be  $\sim 10^{-5}$ , with a stiff dependence on angular separation. The performance of the NIRCam/JWST coronagraph at five microns will depend upon JWST's Airy pattern and phase stability, and these have yet to be determined. Furthermore, the long-wavelength ( $5-28 \mu\text{m}$ ) spectrometer on JWST, MIRI, should be able to achieve planet-star contrasts from  $10^{-4}$  to  $10^{-6}$  in four filters centered around four wavelengths ( $10.65, 11.4, 15.5$  and  $23 \mu\text{m}$ ) with spectral resolutions ( $\frac{\lambda}{\Delta\lambda}$ ) of  $\sim 100$ . The most sensitive contrast will be achieved only at large IWAs near  $\sim 1''$ . Again, putative performance curves for WFIRST/CGI, JWST, and GPI are depicted on Figure 1. Therefore, it is possible that 1) JWST could characterize a nearby, wide-separation exoplanet at  $4-5 \mu\text{m}$  and from  $\sim 10 \mu\text{m}$  to  $\sim 23 \mu\text{m}$ , 2) WFIRST/CGI could do so in the optical, and 3) the combined dataset could constrain planet properties much better than either alone. There are only a few known RV planets with large enough greatest elongations (§3.3), but both GPI/SPHERE (in the H band) and WFIRST are likely to find more. So, the potential of combined WFIRST and JWST data for exoplanet characterization is significant. Since such objects are much brighter in the M band and at longer wavelengths, this is all the more compelling for the young,



and massive (perhaps brown dwarf) targets or discoveries.

## 7. COMMENTS ON INDICES AND RETRIEVAL

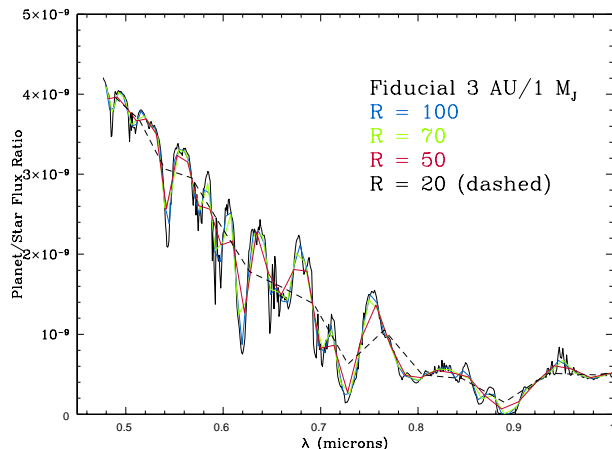


FIG. 19.— A comparison of the planet/star reflection spectrum for a model 1- $M_J$ /5 Gyr giant exoplanet at 3 AU from a G2 V star, as a function of spectral resolution ( $R = \lambda/\Delta\lambda$ ) from 100 to 20.

In advance of freezing the WFIRST coronagraph design, one may ask the question: What spectral resolution in the optical ( $R = \lambda/\Delta\lambda$ ) might be necessary to extract useful information about a giant planet's atmosphere? Below what  $R$  is a spectrum nearly useless? Figure 19 depicts the planet/star flux ratio versus wavelength at various  $R$ s for a representative 1.0  $M_J$  planet at 3.0 AU from a G2V star. A baseline model at  $R \sim 700$  is shown for reference. One can see that the methane and water features for the  $R = 100$  and  $R = 70$  models are easily discernible, but that below these  $R$ s features are washing out. At  $R = 20$ , aside for the general slope of the curve (which can be used to derive gross properties about the underlying cloud and possible chromophore), critical compositional information is quite lost.

Each methane feature of Figure 4 is formed at a different altitude and pressure. Therefore, changing the methane abundance changes the strength of each feature differently. Without clouds, this provides a straightforward way to approximate abundances – various indices (colors) calculated from the ratios of the depths of different methane spectral features (around  $\sim 0.62 \mu\text{m}$ ,  $\sim 0.74 \mu\text{m}$ ,  $\sim 0.81 \mu\text{m}$ , and  $\sim 0.89 \mu\text{m}$ ) and adjacent continua can be calibrated to yield an average methane abundance from observations. Figure 20 demonstrates the general dependence of the geometric albedo upon metallicity of a homogeneous atmosphere. Though these models are cloud-free, this figure suggests that higher metallicities result in lower albedos, particularly longward of  $\sim 0.6 \mu\text{m}$ . This figure also suggests that various flux ratios, particularly between  $\sim 0.5 - 0.6 \mu\text{m}$  and/or  $\sim 0.82$  and  $\sim 0.94 \mu\text{m}$ , can be metallicity indices. Note that the higher metallicity models on this plot seem to recapitulate the behavior of the albedo spectra at longer wavelengths of Uranus and Neptune (Figure 16) vis à vis those of Jupiter and Saturn.

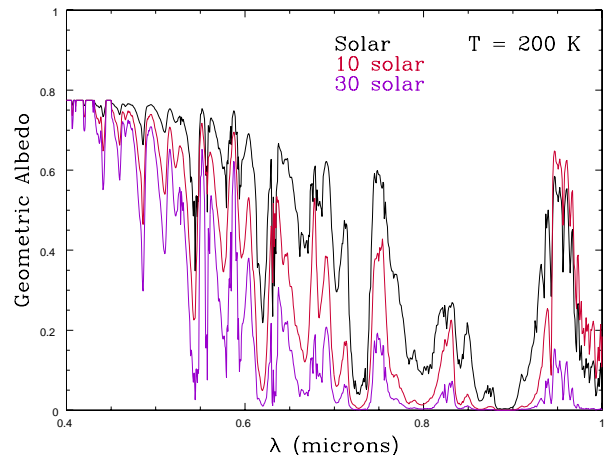


FIG. 20.— A study of planet geometric albedo spectra for homogeneous model giant exoplanet atmospheres at  $T = 200$  K as a function of atmospheric metallicity (1, 10, and  $30\times$  solar). These models are cloud-free and use opacities at a pressure of 0.5 atmospheres. Gas-phase opacities are not strong functions of pressure, but are strong functions of temperature and metallicity.

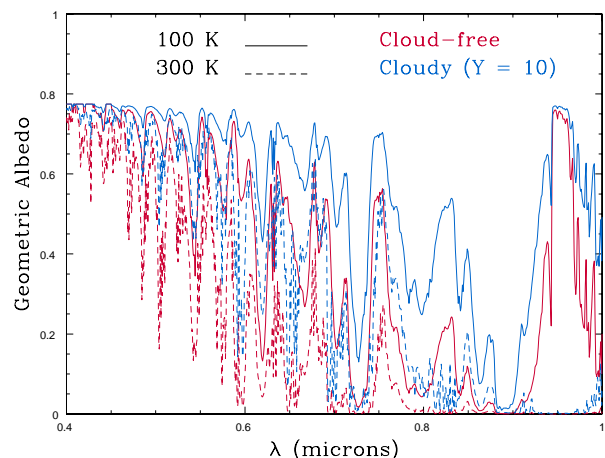


FIG. 21.— A set of model geometric albedo spectra, demonstrating the generally strong dependence of reflection albedos upon temperature or the presence of clouds. A metallicity of  $10\times$  solar and a pressure of 0.5 atmospheres are assumed. The parameter  $Y$  here is the ratio of the cloud scattering opacity to the molecular Rayleigh scattering opacity and values of  $Y = 0$  and  $Y = 10$  are included for comparison. This ratio is roughly constant for homogeneously-distributed water or ammonia clouds consisting of small particles, but the use of the  $Y$  parameter here is meant merely to demonstrate the general albedo spectrum behavior with cloud opacity. (We note that the scattering albedo of water droplets in the optical is very close to one.) Also shown are models with  $T = 100$  K and  $T = 300$  K to depict the general dependence of the albedo spectrum upon atmospheric temperature. The higher the temperature, the lower the albedo, particularly longward of  $\sim 0.65 \mu\text{m}$  and around  $\sim 0.95 \mu\text{m}$ .

Figure 21 communicates the rough dependence of the geometric albedo upon both atmospheric temperature and cloud thickness. For these example models, a metallicity of  $10\times$  solar and a pressure of 0.5 atmospheres are assumed. We note that gas-phase scattering albedos ( $\omega$ )

are not strong functions of pressure, but as Figure 21 clearly indicates the geometric albedo of a giant exoplanet can be a stiff function of its atmospheric temperature, particularly longward of  $\sim 0.65 \mu\text{m}$ . Figure 21 also attempts to communicate the general influence of clouds on reflectivity. The presence of clouds requires that multiple indices be used simultaneously to break the approximate degeneracy that will result from the effect of clouds on planet/star flux ratios. In this case (perhaps generic), a single index or color measurement is less useful, since some bands can be saturated and the effects of clouds are *a priori* not known. Hence, multiple indices are suggested for simultaneous retrieval of metallicity, atmospheric temperature, and cloud character. The latter could involve cloud top pressure and modal particle sizes, but could also involve cloud type. Since higher temperature atmospheres will also be thermal emitters longward of  $\sim 0.8 \mu\text{m}$ , a combination of indices that involves the  $\sim 0.9\text{--}1.0 \mu\text{m}$ ,  $\sim 0.8\text{--}0.85 \mu\text{m}$ ,  $\sim 0.65\text{--}0.7 \mu\text{m}$ , and  $\leq 0.6 \mu\text{m}$  broad bands, and/or indices constructed from fluxes in and out of the methane features to include the associated continua, should allow one simultaneously to break various approximate temperature, metallicity, and cloud degeneracies. In short, the key is multiple “color” indices, strategically placed. As articulated in §2, §2.1, §3.4, and §5, phase and polarization data would further improve the scientific return of a focussed campaign of exoplanet remote sensing by WFIRST.

## 8. SUMMARY AND CONCLUSIONS

Here, we summarize the salient conclusions we have reached in this quick study concerning the scientific potential of high-contrast giant exoplanet measurement in the optical, as it pertains to the WFIRST-AFTA coronagraph initiative. A more detailed multi-parameter exploration is certainly necessary to flesh out the full range of potential signatures and diagnostics of giant exoplanet atmospheres using optical coronagraphy. However, despite its brevity, this quick study highlights 1) the variety expected both for wide-separation giant planet atmospheres, 2) their discriminating planet/star ratio spectra, and 3) the rich potential for atmospheric characterization afforded by optical coronagraphy with WFIRST/CGI’s planned specifications. In bulletized form, we find that:

- Albedos of giant exoplanets can be quite large and are strongly wavelength- and orbital-distance-dependent. Shortward of  $\sim 1.0 \mu\text{m}$ , most giant exoplanets reflect incident light to a larger degree in the *B* and the *V* bands than in the *R* or *I* bands.
- Because the methane abundances and the presence and properties of clouds are functions of temperature, the albedo spectrum is a non-monotonic function of planet mass and age, orbital distance, stellar type, and planet elemental composition.
- In the WFIRST/CGI band between  $\sim 0.4 \mu\text{m}$  and  $\sim 1.0 \mu\text{m}$ , the flux ratios for orbital distances from  $\sim 1 \text{ AU}$  to  $\sim 10 \text{ AU}$  and for planet masses from  $0.5 M_J$  to  $10 M_J$  can vary from  $\sim 10^{-7}$  to  $\sim 10^{-10}$ .

- The optical has prominent and diagnostic methane features near  $\sim 0.62 \mu\text{m}$ ,  $\sim 0.74 \mu\text{m}$ ,  $\sim 0.81 \mu\text{m}$ , and  $\sim 0.89 \mu\text{m}$ ; ammonia features at  $\sim 0.65 \mu\text{m}$  and  $\sim 0.79 \mu\text{m}$ ; and a broad water band at  $\sim 0.94 \mu\text{m}$ , all of which vary in strength with orbital distance, elemental abundances, and planet mass and age.
- The planet/star flux ratio does not follow an inverse-square law with orbital distance, and the deviations from such behavior are functions of wavelength and composition.
- Generally (but not universally), the optical albedo increases significantly with increasing orbital distance from  $\sim 1.0 \text{ AU}$  to  $15 \text{ AU}$ . With the onset of water clouds, the optical albedo rises and the onset and thickening of reflective ammonia clouds at still larger orbital distances results in the highest albedos at most optical and near-infrared wavelengths.
- Since older planets have clouds with higher column depths, giant planet albedos are expected to increase with age. Conversely, since higher mass giants have higher surface gravities, which result in clouds with lower column depths, at shorter wavelengths higher-mass giant exoplanets are expected to have slightly smaller albedos and planet/star flux ratios. This flux trend with planet mass is opposite to that expected at the longer wavelengths (still shortward of the  $\sim 1.0 \mu\text{m}$ ) accessible to WFIRST/CGI.
- The effects of clouds on the optical and infrared can anti-correlate, with the optical fluxes increasing and the near infrared fluxes decreasing with increasing cloud depth.
- All else being equal, the higher the metallicity or the higher the atmospheric temperature, particularly for cloud-free models, the lower the geometric albedo. Clouds mute this effect, but its general operation makes the  $0.94\text{-}\mu\text{m}$  water band and the  $\sim 0.65\text{--}0.8 \mu\text{m}$  fluxes, in particular, useful functions of metallicity and diagnostics of atmospheric temperature.
- Theory suggests that water clouds form around a G2V star exterior to a distance near  $1.5 \text{ AU}$ , whereas ammonia clouds form around such a star exterior to a distance near  $4.5 \text{ AU}$ . Jupiter and Saturn are consistent with these expectations, but WFIRST/CGI data as a function of orbital distance will allow us to explore this fundamental expectation concerning cloud formation in planetary atmospheres for a much larger planet sample and beyond the solar system.

- Small cloud particle sizes ( $\sim 1 \mu\text{m}$ ) produce higher planet/star flux ratios than large particle sizes ( $\sim 100 \mu\text{m}$ ) at most optical and near-IR wavelengths.
- Planet/star flux ratios are strong functions of orbital phase, inclination, and eccentricity. At optical wavelengths, highly-inclined circular orbits, are three to four times brighter near full phase than near greatest elongation.
- Giant exoplanets in elliptical orbits can undergo major atmospheric compositional changes, which may have significant effects on their light curves. Additionally, elliptical orbits generally introduce a pronounced offset between the time of the light curve peak and the time of full planetary phase.
- Thermal emission, not reflection, could dominate longward of  $\sim 0.7\text{--}0.8 \mu\text{m}$  for massive and/or young giant exoplanets. This will increase the associated flux, change the slope of the continuum at these longer wavelengths, still within WFIRST/CGI's reach, and could mute the phase dependence of the corresponding emission in a fashion diagnostic of mass and age.
- Whether there is a phase dependence and a day/night contrast in this thermal component will depend upon the depth of the radiative/convective transition, itself dependent upon the orbital distance and/or stellar flux level. A shallow transition (expected for large separations) will diminish the day/night contrast of thermal flux and the corresponding phase light curve variation, while a deep transition (expected for closer planets) will create a day/night contrast at thermal wavelengths. Hence, for more massive planets, the phase curve at longer wavelengths is a signature of the mechanism of day/night heat redistribution, either by zonal atmospheric flows or by deep convection. Such measurements for many targets could reveal the orbital distance of this important transition for a given primary star type.
- Chromophores might suppress the flux shortward of  $\sim 0.6 \mu\text{m}$ . If present, as they are in Jupiter and Saturn but are not in Uranus and Neptune, the associated change in the slope of the albedo function and flux alone will reveal their presence. Hence, correlations of the red/blue colors of WFIRST/CGI targets with stellar type and metallicity, planet mass, and/or orbital distance could teach us about the associated chemistry of not only giant exoplanets, but of the solar-system giants as well.
- Planetary polarization at a given wavelength is likely to be a more diagnostic function of phase than the total intensity light curve in probing cloud and haze properties and positions in gas giant atmospheres.
- Polarization for gas molecules and for typical cloud and aerosol particles are distinctly different, making full linear Stokes polarization a valuable tool for determining the presence and nature of aerosol particles.
- Peak exoplanet polarizations can be large, ranging from  $\sim 10\%$  to  $\sim 90\%$ , and vary diagnostically with wavelength.
- At shorter optical wavelengths, polarization generally contains information about the upper planet atmosphere, while at longer wavelengths clouds deeper in the atmosphere are probed. Hence, polarization color indices (for example, comparing  $R$  and  $B$ , or  $R$  and  $I$ -band) can reveal the presence, thickness, and optical depth of a Rayleigh scattering layer.
- There is a phase angle at which the polarized flux (as opposed to the polarized fraction) is a maximum. For conservative Rayleigh scattering, this angle is  $\sim 65^\circ$ , but it is generally larger for haze particles. Hence, this angle alone can be used as a diagnostic of the presence of aerosols.
- Since polarization is a relative measure, and, hence, perhaps more intrinsically accurate, the degree of polarization in both spectral bands and the continuum depends strongly upon atmospheric composition and structure.
- When combining geometric albedo and polarization data as a function of wavelength simultaneously (for a known orbital phase), one should be able to break various approximate degeneracies introduced by the presence of aerosols.
- Tropospheric and stratospheric cloud models might be distinguished by the line-to-continuum polarization ratios. Though the fractional polarization can be large in strong absorption bands, while the flux itself is small (due to absorption), the continuum does not suffer from this effect. Hence, both flux and polarization ratio indices between the absorption bands and the adjacent continuum are useful diagnostics of scattering cloud depth, the presence of aerosols, particle size and make-up, and the relative contribution of Rayleigh scattering.
- The sharpness of the phase variation in the polarization increases markedly for larger particles or shorter wavelengths, and this can be used to directly constrain particle size.

- The robustness of the qualitative single-scattering polarization in the context even of multiple scattering suggests that spherical droplets could imprint rainbow and/or glory effects as a function of wavelength.
- At longer wavelengths, and for more massive and/or younger giant planets, the fact that the flux could be thermal erases the polarization and its orbital phase dependence. Thus, the polarization contrast between the short and long WFIRST/CGI wavelength bins, and its variation with phase, should be diagnostic functions of the temperature of the planet's atmosphere and of planet mass and/or age.

The author would like to thank David Sudarsky, Nikku Madhu, Wes Traub, Ivan Hubeny, Jonathan Lunine, Mark Marley, Glenn Schnieder, Brian MacIntosh, Jim Breckinridge, Hans-Martin Schmid for collaborations, conversations, and insights and acknowledges JPL for support during the execution of this project. He gratefully acknowledges NASA's Exoplanet Exploration Program for supporting this study on behalf of the WFIRST/AFTA Science Definition Team and the Exo-S and Exo-C Science and Technology Definition Teams.



## REFERENCES

- Beuzit, J.-L. et al. SPHERE: a planet finder instrument for the VLT. in *Ground-based and Airborne Instrumentation for Astronomy II*. Edited by McLean, Ian S.; Casali, Mark M. *Proc. SPIE* 7014:701418-701418-12 (2008)
- Barman, T., Macintosh, B., Konopacky, Q.M., & Marois, C. Clouds and Chemistry in the Atmosphere of Extrasolar Planet HR8799b. *Astrophys. J.*, 733, article id. 65, 18 pp. (2011)
- Buenzli, E. & Schmid, H.M. 2009, *Astron. Astrophys.*, 504, 259
- Burrows, A., Marley, M., Hubbard, W. B., Lunine, J. I., Guillot, T., Saumon, D., Freedman, R., Sudarsky, D., & Sharp, C. 1997, "A Non-Gray Theory of Extrasolar Giant Planets and Brown Dwarfs," *Astrophys. J.*, 491, 856
- Burrows, A. & Sharp, C.M. 1999, "Chemical Equilibrium Abundances in Brown Dwarf and Extrasolar Giant Planet Atmospheres," *Astrophys. J.*, 512, 843.
- Burrows, A., Sudarsky, D., and Lunine, J.I. 2003, "Beyond the T Dwarfs: Theoretical Spectra, Colors, and Detectability of the Coolest Brown Dwarfs," *Astrophys. J.*, 596, 587
- Burrows, A., Sudarsky, D., & Hubeny, I. 2004, "Spectra and Diagnostics for the Direct Detection of Wide-Separation Extrasolar Giant Planets," *Astrophys. J.*, 609, 407
- Burrows, A. A theoretical look at the direct detection of giant planets outside the Solar System. *Nature*, 433, 261-268 (2005)
- Cooper, C.S., Sudarsky, D., Milsom, J.A., Lunine, J.I., & Burrows, A. 2003, "Modeling the Formation of Clouds in Brown Dwarf Atmospheres," *Astrophys. J.*, 586, 1320
- Deming, D. et al. Discovery and Characterization of Transiting Super Earths Using an All-Sky Transit Survey and Follow-up by the James Webb Space Telescope. *PASP*, 121, 952-967 (2009)
- Deirmendjian, D. 1964, *Appl. Opt.*, 3, 187
- Deirmendjian, D. 1969, *Electromagnetic scattering on spherical polydispersions*, New York, NY (USA): Elsevier Scientific Publishing
- Fluri, D.M. & Berdyugina, S.V. 2010, *Astron. Astrophys.*, 512, A59 pp. 1-12
- Hansen, J.E. & Hovenier, J.W. 1971, *J. Quant. Spectrosc. Radiat. Transfer*, 11, 809
- Hansen, J.E. & Hovenier, J.W. 1974, *J. Atmos. Sci.*, 31, 1137
- Hansen, J.E. & Travis, L.D. 1974, *Space Sci. Rev.*, 16, 527
- Karkoschka, E. 1994, *Icarus*, 111, 174
- Karkoschka, E. 1998, *Icarus*, 133, 134
- Khare, B.N. et al. 1984, *Icarus*, 60, 127
- Kurucz, R. 1994, "Solar abundance model atmospheres for 0,1,2,4,8 km/s," *Kurucz CD-ROM No. 19*, (Cambridge: Smithsonian Astrophysical Observatory)
- Lagrange, A.M. et al. A probable giant planet imaged in the  $\beta$  Pictoris disk. VLT/NaCo deep L'-band imaging. *Astron. Astrophys.*, 493, L21-L25 (2009)
- Macintosh, B. et al. The Gemini Planet Imager: from science to design to construction. in *Adaptive Optics Systems*. Edited by Hubin, Norbert; Max, Claire E.; Wizinowich, Peter L. *Proc. SPIE* 7015:701518-701518-13 (2008)
- Madhusudhan, N., & Burrows, A. Analytic Models for Albedos, Phase Curves, and Polarization of Reflected Light from Exoplanets. *Astrophys. J.*, 747, 25-40 (2011)
- Madhusudhan, N., Burrows, A., & Currie, T. Model Atmospheres for Massive Gas Giants with Thick Clouds: Application to the HR 8799 Planets. *Astrophys. J.*, 737, 34-48 (2011)
- Marley, M.S., Gelino, C., Stephens, D., Lunine, J.I., & Freedman, R. Reflected Spectra and Albedos of Extrasolar Giant Planets. I. Clear and Cloudy Atmospheres. *Astrophys. J.*, 513, 879-893 (1999)
- Marois, C. et al. Direct Imaging of Multiple Planets Orbiting the Star HR 8799. *Science*, 322, 1348-1352 (2008)
- Marois, C., Zuckerman, B., Konopacky, Q.M., Macintosh, B., & Barman, T. Images of a fourth planet orbiting HR 8799. *Nature*, 468, 1080-1083 (2010)
- Oppenheimer, B.R. & Hinkley, S. 2009, "High-Contrast Observations in Optical and Infrared Astronomy," *Ann. Rev. Astron. Astrophys.*, 47, 253
- Patten, B. et al. 2006, "Spitzer IRAC Photometry of M, L, and T Pope, S. K., Tomasko, M. G., Williams, M. S., Perry, M. L., Dooze, L. R., & Smith, P. H. 1992, *Icarus*, 100, 203
- Rages K.A., Galileo Imaging Team 1997, *AAS DPS*, 29, 19.17
- Rages K.A., Pollack, J.B., & Smith, P.H. 1983, *J. Geophys. Res.*, 88, 8721
- Sagan, C. & Khare, B.N. 1979, *Nature*, 277, 102-107
- Schmid, H.M. et al. 2006, "Search and Investigation of Extra-solar Planets with Polarimetry," in *Proceedings on Direct Imaging of Exoplanets: Science & Techniques*, IAU Colloquium No. 200, 2005), doi:10.1017/S1743921306009252
- Skrutskie, M.F. et al. "The Large Binocular Telescope mid-infrared camera (LMIRcam): final design and status," in *Ground-based and Airborne Instrumentation for Astronomy III*. Edited by McLean, Ian S.; Ramsay, Suzanne K.; Takami, Hideki. *Proceedings of the SPIE*, Volume 7735, article id. 77353H, 11 pp. (2010).
- Sharp, C.M. & Burrows, A. 2007, "Atomic and Molecular Opacities for Brown Dwarf and Giant Planet Atmospheres," *Astrophys. J. Suppl. Ser.*, 168, 140
- Smith, P. H. 1986, *Icarus*, 65, 264
- Smith, P.H. & Tomasko, M.G. (1984), *Icarus*, 58, 35
- Spergel, D.N., Gehrels, N. et al. Wide-Field InfraRed Survey Telescope – Astrophysics Focused Telescope Assets WFIRST-AFTA Final Report. <http://arxiv.org/abs/1305.5422> (astro-ph/1305.5422) (2013)
- Stam, D.M., Hovenier, J.W., & Waters, L.B.F.M. 2004, *Astron. Astrophys.*, 28, 663-672
- Sudarsky, D., Burrows, A., & Pinto, P. 2000, "Albedo and Reflection Spectra of Extrasolar Giant Planets," *Astrophys. J.*, 538, 885
- Sudarsky, D., Burrows, A., and Hubeny, I. 2003, "Theoretical Spectra and Atmospheres of Extrasolar Giant Planets," *Astrophys. J.*, 588, 1121
- Sudarsky, D., Burrows, A., Hubeny, I., & Li, A. 2005, "Phase Functions and Light Curves of Wide-Separation Extrasolar Giant Planets," *Astrophys. J.*, 627, 520
- Suzuki, R. et al. Performance characterization of the HiCIAO instrument for the Subaru Telescope. *Proceedings of the SPIE*, 7735, article id. 773530, 13 pp. (2010)
- Tomasko, M.G. & Smith, P.H. 1982, *Icarus*, 51, 65
- West, R.A., Hart, H., Simmons, K.E. et al. 1983, *J. Geophys. Res.*, 88, 8699
- West, R. A., Strobel, D. F., & Tomasko, M. G. 1986, *Icarus* 65, 161
- West, R.A. & Smith, P.H. 1991, *Icarus*, 90, 330
- Wiktorowicz, S.J. 2009, *Astrophys. J.*, 696, 1116

TABLE 1  
MODEL DATA FOR SPECIFIC RV GAS GIANTS

| Planet            | Max. separation (") | star | a (AU) | d (pc) | P (yrs.) | $M_p \sin(i)$ ( $M_J$ ) | $\log_{10} g$ (cgs) |
|-------------------|---------------------|------|--------|--------|----------|-------------------------|---------------------|
| 55 Cnc d          | 0.44                | G8V  | 5.9    | 13.4   | 14.7     | 4.05                    | 4.30                |
| 47 UMa c          | 0.28                | G0V  | 3.73   | 13.3   | 7.10     | 0.76                    | 3.48                |
| Gl 777A b         | 0.23                | G6V  | 3.65   | 15.9   | 7.15     | 1.15                    | 3.48                |
| $\nu$ And d       | 0.19                | F8V  | 2.50   | 13.5   | 3.47     | 4.61                    | 4.30                |
| HD 39091b         | 0.16                | G11V | 3.34   | 20.6   | 5.70     | 10.3                    | 4.48                |
| 47 UMa b          | 0.16                | G0V  | 2.09   | 13.3   | 2.98     | 2.54                    | 3.78                |
| $\gamma$ Cephei b | 0.15                | K2V  | 1.8    | 11.8   | 2.5      | 1.25                    | 3.60                |
| 14 Her b          | 0.15                | K0V  | 2.5    | 17     | 4.51     | 3.3                     | 3.90                |

TABLE 2  
GEOMETRIC ALBEDO ( $A_g$ ), POLARIZATION FRACTION MAXIMUM ( $P_{\max}$ ), AND  $\theta_{\max}$  FOR VECTOR RAYLEIGH SCATTERING  
OFF A SPHERICAL PLANET, AS A FUNCTION OF SCATTERING ALBEDO ( $\omega$ )

| $\omega$ | $A_g$  | $P_{\max}$ | $\theta_{\max}$ |
|----------|--------|------------|-----------------|
| 0.100    | 0.0198 | 0.9787     | 90.0            |
| 0.200    | 0.0420 | 0.9513     | 89.0            |
| 0.300    | 0.0672 | 0.9216     | 89.0            |
| 0.400    | 0.0963 | 0.8884     | 90.0            |
| 0.500    | 0.1304 | 0.8498     | 90.0            |
| 0.600    | 0.1716 | 0.8038     | 90.0            |
| 0.700    | 0.2234 | 0.7472     | 90.0            |
| 0.800    | 0.2928 | 0.6750     | 90.0            |
| 0.900    | 0.3999 | 0.5733     | 91.0            |
| 0.980    | 0.5857 | 0.4320     | 92.0            |
| 0.990    | 0.6403 | 0.3995     | 93.0            |
| 0.995    | 0.6823 | 0.3772     | 93.0            |
| 1.000    | 0.7977 | 0.3263     | 95.0            |